Optical Fiber Photoacoustic Gas Sensor With Graphene Nano-Mechanical Resonator as the Acoustic Detector

Yanzhen Tan, Congzhe Zhang, Wei Jin, *Senior Member, IEEE*, Fan Yang, Hoi Lut Ho, and Jun Ma

(Invited Paper)

Abstract—We report an all-optical fiber photoacoustic gas sensor with a graphene nano-mechanical resonator as the acoustic detector. The acoustic detector is a Fabry–Perot interferometer formed by attaching a 100-nm-thick, 2.5-mm-diameter multilayer graphene diaphragm to a hollow cavity at the end of a single-mode optical fiber. By operating at one of the mechanical resonances of the diaphragm, the sensitivity for acoustic detection is enhanced and a noise equivalent minimum detectable pressure of 2.11 μPa/Hz$^{1/2}$ at 10.1 kHz is demonstrated. Detection of acetylene gas is demonstrated with a distributed feedback semiconductor laser tuned to the P(9) absorption line of acetylene and a lower detection limit of 119.8 parts-per-billion (ppb) is achieved with 123.9-mW pump power. Theoretical analysis shows that by increasing the Q-factor of the resonator, which may be achieved by operating at low gas pressures, ppb level gas detection is possible. The all-fiber photoacoustic gas sensor is immune to electromagnetic interference, safe in flammable and explosive environment, and would be ideally suited for remote, space-limited applications and for multi-point detection in a multiplexed fiber optic sensor network.

Index Terms—Gas sensor, multilayer graphene, nano-mechanical resonator, optical fiber sensor, photoacoustic spectroscopy.

I. INTRODUCTION

TRACE gas detection is of great importance in many areas, such as breath analysis for medical diagnosis, environmental atmospheric monitoring, and national security applications. Photoacoustic spectroscopy (PAS), in which periodic light absorption of gas molecules is converted into acoustic pressure wave via the photoacoustic (PA) effect, is a powerful spectroscopic technique for trace gas analysis [1]–[3]. Gas detection based on PAS may be dated back to 1938 where a blackbody emitter was used as the light source to excite the generation of acoustic wave [4]. In 1968, a CO_2 laser was used as the light source for PA detection of carbon dioxide [5]. Since then, various laser-based systems with wavelength ranging from mid- to near-infrared have been reported for the detection of different gases [6]–[9]. These systems use a PA cell in which light absorption of gas takes place, and the acoustic signal is generated and detected. To generate a higher level acoustic signal, a high power laser source with its wavelength tuned to a stronger gas absorption line is needed. The PA signal can be further enhanced by using an acoustic resonator to form a resonant PA cell [10], [11]. By modulating the intensity/wavelength of the laser at a frequency matched to the resonant frequency of the acoustic resonator, an amplified PA signal is generated due to resonant buildup and acoustic energy accumulation within the gas cell. A variety of PA resonators operating on longitudinal, azimuthal and radial resonances have been developed for trace gas detection [1], [12]–[23].

The generation of acoustic wave can also be enhanced by using optical multi-pass [24]–[27] and cavity enhanced [28], [29] PA cells. In a multi-pass system, light beam is reflected multiple times over a certain detection area, resulting in increased light absorption and hence the larger acoustic energy over the area. By tuning the laser wavelength to a cavity mode of a high-finesse optical cavity, optical power could be coupled into the cavity efficiently, leading to high optical power buildup and yielding a stronger PA signal within the cavity.

For acoustic detection, various techniques have been used, including capacitive microphones [21]–[23], resonant quartz tuning forks [3], [30]–[35], and micro-cantilever beams in combination with optical interferometry [36]–[40]. With these acoustic detectors, gas detection down to sub-parts-per-million (sub-ppm) or parts-per-billion (ppb) level has been achieved. Table I summarizes the lower detection limits of some of the reported PAS systems operating at the near infrared wavelength region. It lists the system performance in terms of noise equivalent concentration (NEC) and normalized noise equivalent absorption coefficient (NNEA), and the definitions of which are given in Section II. The NNEA is independent of the gas species

Y. Tan, W. Jin, F. Yang, and H. L. Ho are with the Department of Electrical Engineering, The Hong Kong Polytechnic University, Hung Hom, Kowloon, Hong Kong (e-mail: yanzhen.tan@connect.polyu.hk; wei.jin@polyu.edu.hk; ee.yangfan@connect.polyu.hk; eehlho@polyu.edu.hk).

C. Zhang is with Beihang University, Beijing 100191, China and also with the Department of Electrical Engineering, The Hong Kong Polytechnic University, Hung Hom, Kowloon, Hong Kong (e-mail: congzhe.zhang@polyu.edu.hk).

J. Ma is with Washington University at St. Louis, St. Louis, MO 63130 USA (e-mail: eejun.ma@connect.polyu.hk).

Color versions of one or more of the figures in this paper are available online at http://ieeexplore.ieee.org.

TABLE I
DETECTION LIMITS OF PAS GAS SENSORS

Gas type	Wavelength (μm)	Detection Technique	Pressure (Torr)	Power (mW)	NNEA (cm^{-1}WHz$^{-1/2}$)	NEC (ppm)	Integration time (s)	PA resonant tube
NH$_3$ [21]	1.532	Microphone	100	500	1.5×10^{-9}	0.006	10	Yes
C$_2$H$_2$ [22]	1.511	Microphone	760	3.5	4×10^{-8}	10	0.003	Yes
NH$_3$ [23]	1.5317	Microphone	760	500	Not stated	0.003	0.1	Yes
CH$_4$ [30]	1.6668	QEPAS	375	2	1.2×10^{-7}	Not stated	1	Yes
NH$_3$ [31]	1.5317	QEPAS	60	38	7.2×10^{-9}	0.65	1	Yes
H$_2$O[33]	1.3963	QEPAS	760	8	5.9×10^{-9}	Not stated	1	Yes
C$_2$H$_2$ [35]	1.5316	QEPAS	770	37	3.3×10^{-9}	0.085	1	Yes
CO$_2$ [37], [38]	1.5720	Cantilever-based	190	50	4.9×10^{-9}	7.2	Not stated	No
CO$_2$ [39]	1.5720	Cantilever-based	760	30	1.7×10^{-10}	1.9	2.6	No

QEPA, Quartz-enhanced photoacoustic spectroscopy; NNEA, Normalized noise equivalent absorption coefficient; NEC, noise equivalent concentration.

and provides a common basis for comparison of the various PAS systems. However, most of the acoustic detectors used electrical cables for signal transmission which limits their applications in remote detection and in environments with high electromagnetic interference. These limitations may be overcome by the employment of optical fibers and fiber-based technologies.

Leslie *et al.* reported the first optical fiber spectrophone for the detection of PA wave in 1981 [41]. Later, Breguet *et al.* demonstrated an optical-fiber microphone formed by winding a fiber coil on a thin plate as one arm of a Michelson interferometer to detect the acoustic signal and achieved a lower detection limit of 14 ppb of ethanol and ozone vapor [42]. Over the past decade, significant work has been done in developing miniature fiber-tip Fabry-Perot interferometer (FPI) type microphones [43]–[49]. Fiber-tip FPI pressure/acoustic sensors with thin photonic crystal [46], metal [47], [48], polymer [43], [44] and graphene diaphragms [49] were reported. These optical fiber probes would be ideally suited for space-limited applications such as acoustic detection within a PA cell. Recently, Wang *et al.* reported the use of a diaphragm-based fiber FPI acoustic sensor in combination with an acoustic resonator for acetylene detection. They used a polymer diaphragm with diameter of 4 mm and thickness of 6 μm and achieved a minimum detectable gas concentration of 1.56 ppb with 500 mW of pump laser power [43]. Without using an acoustic resonator, we demonstrated a simple miniature all-fiber PAS gas sensor with a fiber-tip FPI with a 2-μm-thick, 2.75-mm-diameter polymer diaphragm as the acoustic detector [44]. A lower detection limit of 4.3 parts-per-million (ppm) was achieve with an optical power level of only –8 mW. The acoustic sensitivity of the fiber FPI acoustic detector is largely determined by the dimension and the mechanical properties of the diaphragm and would be enhanced by using a thinner and larger diaphragm.

In this paper, we report an all-optical fiber PA gas sensor with a graphene nano-mechanical resonator as acoustic detector and exploit the use of the resonant characteristic of the graphene diaphragm to enhance the sensitivity of gas detection. The basic principle of PAS for gas detection is briefly reviewed in Section II, and the fabrication and characterization of nano-mechanical resonator acoustic detectors are presented in Section III and IV respectively. In Section V, an all-fiber PA gas sensor with the graphene nano-mechanical diaphragm operating at the resonating and non-resonating modes are tested
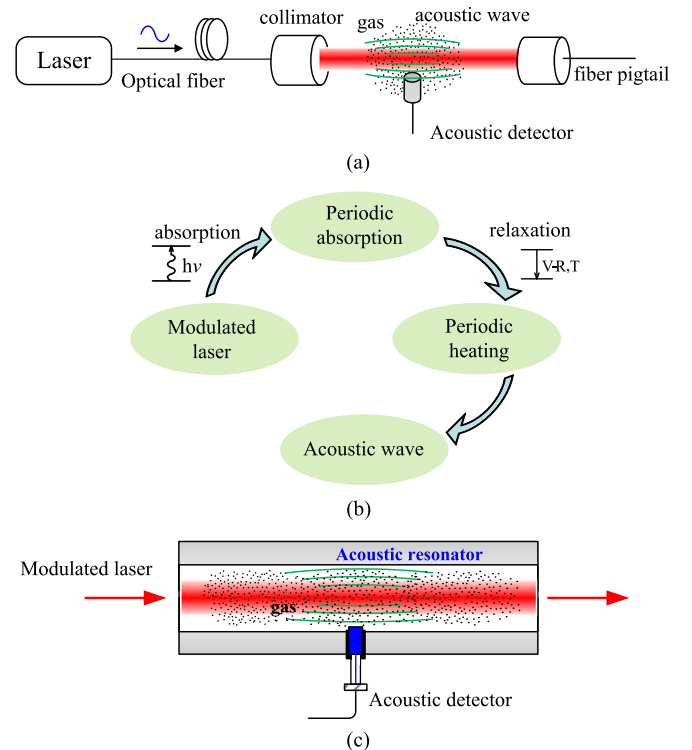

Fig. 1. (a) Principle of gas detection with PAS. (b) Processes of photoacoustic wave generation. (c) PAS with a resonating PA cell.

and compared and the possibility for further performance improvement is discussed.

II. BASICS OF PAS GAS SENSOR

The basics of laser-based PAS gas detection may be explained with the aid of Fig. 1(a) and (b). When a wavelength/intensity modulated pump (excitation) laser beam passes through absorbing gas molecules, the molecules are excited and promoted to a higher energy state. The excited molecules subsequently relax to a lower energy state by non-radiative processes, which result in localized periodic heating via molecular collision and generate an acoustic pressure wave. This magnitude of the acoustic wave is proportional to gas concentration and can be detected by an acoustic detector or a microphone. By use of an additional acoustic resonator and tuning the modulation frequency of the

pump to one of its acoustic resonances shown in Fig. 1(c), the magnitude of the acoustic wave within the resonator could be further enhanced, which enables more sensitive detection of gas concentration.

The output signal from the acoustic detector may be expressed as [22], [50]

$$S = S_m P C_{\text{cell}} \alpha \tag{1}$$

where S_m is the sensitivity of the acoustic detector, P is the power of the pump laser, the PA cell response constant C_{cell} is a scaling factor depending on the PA cell geometry, modulation frequency and measurement conditions. α is the absorption coefficient with $\alpha = N_{\text{tot}} c_m \sigma$, where N_{tot} is the total number density of molecules, c_m is the concentration of the target gas and σ is absorption cross-section. The PA signal is proportional to the gas absorption coefficient α and laser power P, and the use of a well-designed acoustic resonator would also enhance the PA signal through optimizing response constant C_{cell}. The sensitivity of acoustic detection (S_m) may also be enhanced by use of a resonant acoustic detector and operating at its resonant frequency.

The detection limit of a PAS system may be described in terms of noise equivalent concentration of gas (NEC or $c_{m,\text{min}}$) or noise equivalent absorption-coefficient (NEA or α_{min}, in cm^{-1}), which are related by

$$c_{m,\text{min}} = \frac{\alpha_{\text{min}}}{N_{\text{tot}} \cdot \sigma} \tag{2}$$

The value of NEA (α_{min}) is determined by equaling the PA signal power to that of the noise (i.e., SNR = 1). Since the PA signal is proportional to the laser power and the noise power is proportional to the detection bandwidth (assuming white noise), α_{min} is then proportional to the square root of the bandwidth and inversely proportional to the laser power. A normalized NEA (NNEA) measured in cm^{-1}W/Hz$^{1/2}$ can then be defined, which represents the value of NEA normalized to 1 Hz measurement bandwidth and 1 W laser power [50].

III. THE ACOUSTIC DETECTOR

The acoustic detectors used in our study are graphene nano-mechanical resonators located at the ends of optical fibers, as shown in Fig. 2. An optical FPI is formed between the cleaved end of the SMF and the surface of the graphene diaphragm. Acoustic wave applied to the graphene diaphragm drives it back and forth periodically, the periodic deformation modulates the cavity length of the FPI. When a probe light beam is propagating into the FPI, the reflected light intensity will vary periodically, which is detected and processed to recover the acoustic pressure information.

Graphene, a single layer of carbon atoms, is considered as the sensitive diaphragm for pressure sensors because of its ultra-thin thickness, large elastic deformation range and extraordinary stiffness [51]. In recent years, our group has been studying miniature optical fiber acoustic/pressure sensors by using few and multilayer graphene as the sensitive diaphragms [49], [52], [53]. Table II summarizes the characteristic parameters of the graphene diaphragms used in our fiber FPI sensors.
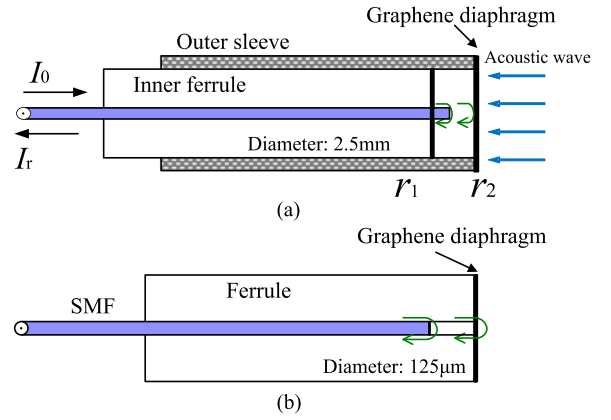

Fig. 2. Schematic diagram of the fiber FPI acoustic detector. (a) a graphene diaphragm with diameter of 2.5 mm covering the endface of a sleeve; (b) a graphene diaphragm with diameter of 125 μm covering the endface of a zirconia ferrule. The green arrows show the reflected probe light waves from the fiber end and the graphene surface.

TABLE II
CHARACTERISTIC PARAMETERS OF THE GRAPHENE DIAPHRAGMS

Graphene	Few-layer		Multilayer	
Type	fiber-tip[52]	ferrule-top[53]	ferrule-top[49]	sleeve-top
Thickness	<1 nm	10~15 nm	100 nm	100 nm
Diameter	25 μm	125 μm	125 μm	2.5 mm

In this section, we focus on two types of acoustic detectors made with 100 nm-thick multilayer graphene diaphragm with different diameter of 2.5 mm and 125 μm, which are shown respectively in Fig. 2(a) and (b). The fabrication process of the 125 μm-diameter diaphragm detector has been described in [49].

As shown in Fig. 2(a), the 2.5 mm-diaphragm acoustic detector comprises of a hollow ceramic sleeve with inner diameter of –2.5 mm, a ceramic ferrule with inner/outer diameter of 125 μm/2.5 mm, a standard single mode fiber (SMF), and a –100-nm-thick multilayer graphene diaphragm. It is fabricated by following a similar procedure described in [54], as illustrated in Fig. 3(a). The difference is that the SMF here was cleaved and the cleaved end and the surface of the graphene diaphragm together formed the FPI. The graphene diaphragm is obtained from a multilayer graphene/Nickel(Ni)/multilayer graphene (MLG/Ni/MLG film) sample (Graphene-supermarket.com). The MLG/Ni/MLG film is firstly flattened by two glass slides and one end of the ceramic sleeve is coated with a thin layer of ultraviolet (UV) curable liquid gel. The top glass slide is then removed and the gel-coated sleeve is compressed onto the flat surface of the sample film. After that, the liquid gel between the sleeve and sample film is cured under the UV light illumination for ~6 hours and the MLG/Ni/MLG film is then firmly stuck to the sleeve end. By immersing the film-stuck sleeve into a ferric chloride (FeCl$_3$) solution, the Ni layer of the MLG/Ni/MLG film can be etched away. The sleeve end is flushed in the de-ionized water to separate the lower MLG film from the sleeve-attached MLG film. The sleeve with MLG
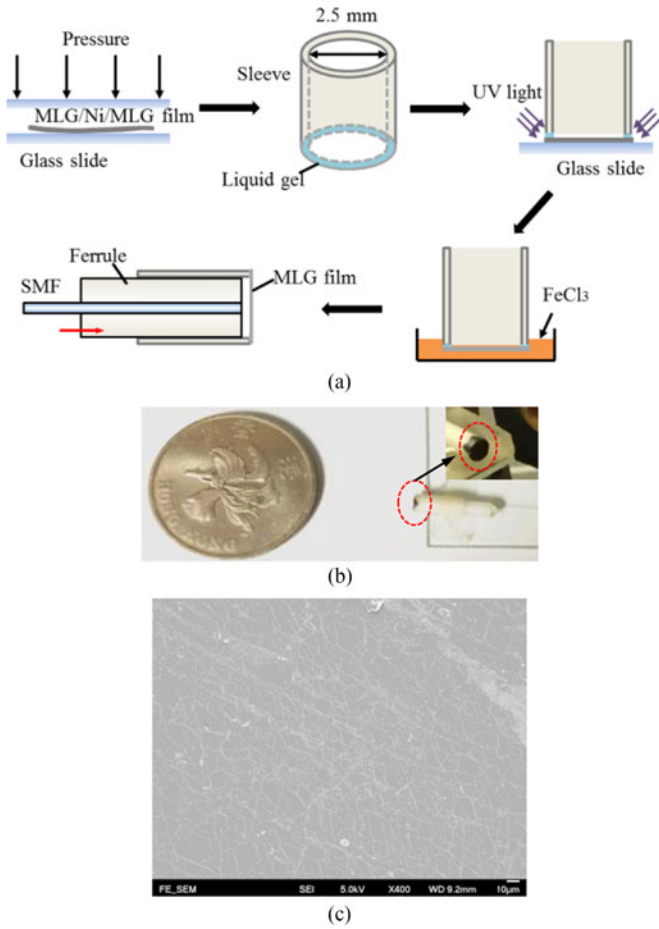
Fig. 3. (a) Fabrication process of the 100 nm-thick, 2.5-mm-diameter MLG diaphragm-based FPI acoustic detector. (b) Photograph of the assembled acoustic detector and the tip of the sensor. (c) SEM image of the graphene film.
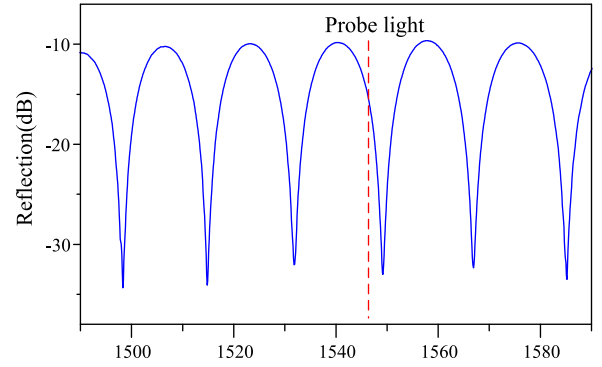

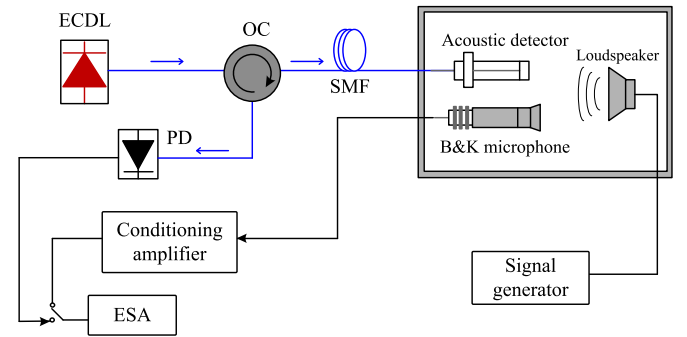Fig. 4. Measured reflection spectrum of the graphene diaphragm-based FPI.

Fig. 5. Experimental setup for testing the performance of the optical fiber acoustic detector. Blue line, optical fiber; black line, electrical cable; ECDL, external-cavity diode laser (the probe); OC, optical circulator; PD, photo-detector; ESA, electrical spectrum analyzer.

film is then dried to remove the residual water. Finally, the ferrule containing a cleaved SMF fixed at its center is inserted into the sleeve and moved slowly toward the MLG film by use of a precision translation stage. The reflective surfaces between the cleaved fiber end and the graphene diaphragm form a low-finesse FPI, and the reflection spectrum is monitored and used to determine the cavity length of the FPI. Once the expected cavity length is achieved, the sleeve is fixed to the ferrule with epoxy. A photograph of the assembled acoustic detector is shown in Fig. 3(b).

The setup used to measure the reflection spectrum of the FPI is a similar to the system described in [55]. Light beam from a broadband light source (Amonics, ALS-CMDM-FA) was propagating into the FPI, and the reflection spectrum was measured by an optical spectrum analyzer (OSA) together with an optical circulator. Fig. 4 shows the measured reflection spectrum of the FPI. The visibility of the interference fringe is −20 dB with a free spectrum range of −17.58 nm around 1550 nm. The corresponding cavity length is then calculated to be 68.33 μm by using $L = \lambda_1 \lambda_2 / 2(\lambda_1 - \lambda_2)$, where λ_1 and λ_2 are the adjacent peak/dip wavelengths in the reflection spectrum.

IV. CHARACTERIZATION OF ACOUSTIC DETECTOR

A. Sensitivity and Frequency Response

The performances of graphene diaphragm-based FPI as acoustic detectors are tested with the experimental setup shown in Fig. 5. The optical fiber acoustic detector under test was placed ∼15 cm from a loudspeaker, which is used as the acoustic source. A calibrated reference microphone was positioned at the symmetry point of the fiber acoustic detector to the central axis of the speaker, and the measured acoustic pressure with the reference microphone is regarded as the same as that incident on the fiber acoustic detector. The optical acoustic detector, the reference microphone and the speaker are all put inside an acoustically isolated chamber.

Light from an external cavity diode laser (ECDL) (Agilent, 81600B) (the probe) is injected to the FPI acoustic detector via an optical circulator (OC). The working wavelength of the probe laser is tuned to the quadrature (Q) point of the interference spectrum to achieve a linear response and to maximize the sensitivity to acoustic pressure [56]. The Q-point is indicated in the reflection spectrum in Fig. 4 (in dB scale) as a dashed red line. The reflected probe light is directed to a photo-detector (PD). The reference microphone was connected with a conditioning amplifier. The electrical outputs from the PD and the
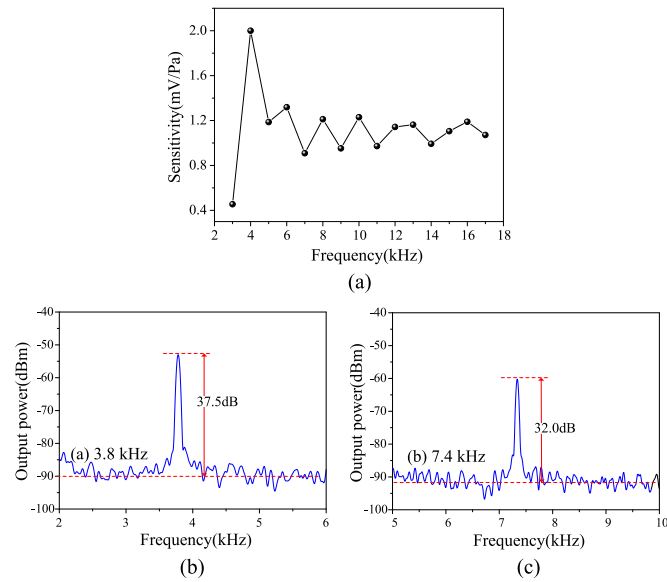
Fig. 6. (a) Frequency response of the fiber FPI with 125-μm-diameter graphene diaphragm. (b) Power spectrum of the photo-detector output when an acoustic pressure level of 35 mPa at 3.8 kHz and (c) 49.5 mPa at 7.4 kHz is applied.
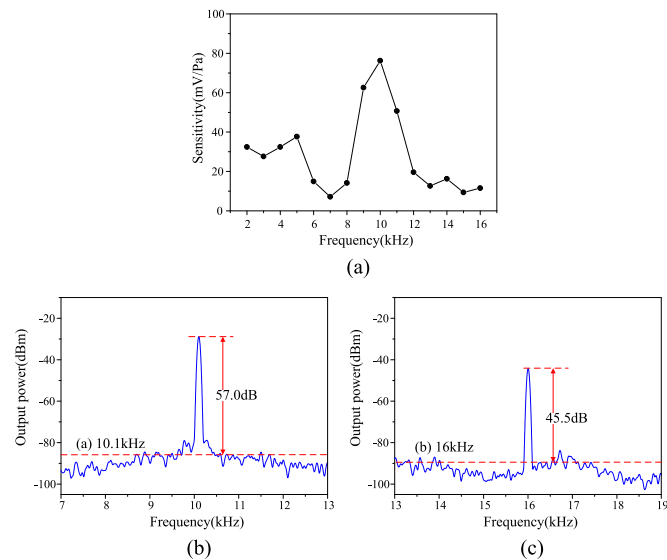

Fig. 7. (a) Frequency response of the FPI with 2.5-mm-diameter graphene diaphragm. (b) Power spectrum of the photo-detector output when an acoustic pressure level of 10.55 mPa at 10.1 kHz and (c) 12.05 mPa at 16.0 kHz is applied.

conditioning amplifier are received and analyzed by a real-time electrical spectrum analyzer (ESA) (Tektronix, 3303A).

The test results for the 125-μm and 2.5-mm diameter FPI acoustic detectors are shown respectively in Figs. 6 and 7. Fig. 6(a) shows the frequency response of the 125-μm-diameter FPI from 3 to 17 kHz, limited by the frequency range of the speaker used. The acoustic pressure sensitivity reaches a maximum value of 2 mV/Pa at ~4 kHz, corresponding to a resonance
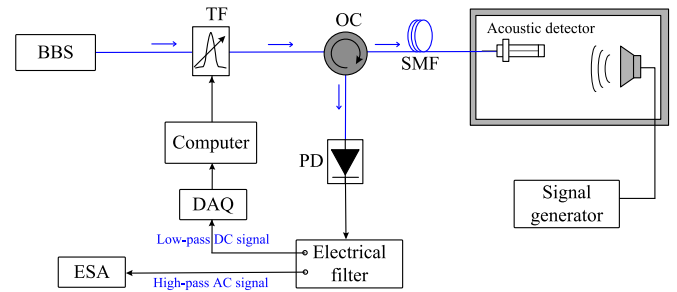

Fig. 8. Experimental setup for testing the long term stability of the acoustic detector. Blue line, optical fiber; black line, electrical cable; BBS, broadband light source; TF, optical tunable filter; OC, optical circulator; PD, photo-detector; DAQ, data acquisition; ESA, electrical spectrum analyzer;

of the graphene diaphragm. Fig. 6(b) and (c) shows respectively the power spectrums of PD output measured with the real-time ESA when acoustic pressure levels of 35.0 mPa at 3.8 kHz and 49.5 mPa at 7.4 kHz are applied. The noise floor is about −90 dBm for a 50 Hz resolution bandwidth. The signal to noise ratios (SNRs) are respectively 37.5 dB and 32 dB for the two cases, corresponding to a noise-limited minimum detectable pressure (MDP) level of 66.0 μPa/Hz$^{1/2}$ at 3.8 kHz and 175.8 μPa/Hz$^{1/2}$ at 7.4 kHz.

The frequency response of the FPI with 2.5-mm-diameter diaphragm is shown in Fig. 7(a). The acoustic pressure sensitivity reaches the maximum value of 80 mV/Pa when operating the graphene diaphragm at resonance (–10.1 kHz). The power spectrum of the photo-detector output for the applied acoustic pressure of 10.55 mPa at 10.1 kHz and 12.05 mPa at 16.0 kHz are shown in Fig. 7(b) and (c), respectively. The noise floor is about −90 dBm for a 50 Hz resolution bandwidth. The SNRs for the two cases are 57.0 dB and 45.5 dB, corresponding respectively to a noise-limited MDP level of 2.11 μPa/Hz$^{1/2}$ at 10.1 kHz and 9.05 μPa/Hz$^{1/2}$ at 16.0 kHz. The value at 10.1 kHz is better than the commercial B&K4189 microphone (–8 μPa/Hz$^{1/2}$), and the MDP at resonance is – 4 times better than off resonance. Moreover, the MDP level of the 2.5-mm-diaphragm acoustic detector is 31 times better than that of the 125-μm-diameter one, showing straightforward sensitivity improvement for graphene diaphragm with a larger diameter, which is in agreement with the model in Ref. [49].

B. Long Term Stability

As mentioned earlier, the wavelength of the probe laser for acoustic detection should be tuned to the *Q*-point of the interference spectrum to achieve a linear response and maximize the sensitivity. However, it was found that operating point often drift due to environmental perturbation such as background pressure change, which leads to long term instability of the demodulation system.

We carried out investigation on the stability of the acoustic detector with another 2.5-mm-diameter diaphragm using the system shown in Fig. 8. The system is similar to the one shown in Fig. 5 but the ECDL is replaced by a board band source (BBS)
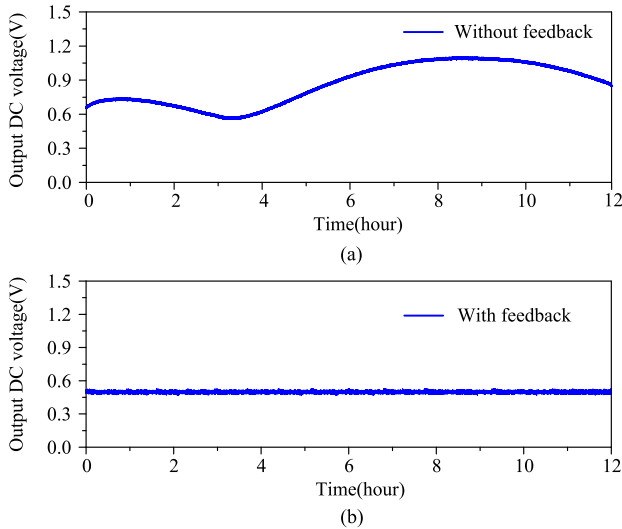
Fig. 9. DC output voltage recorded over 12 hours. (a) without feedback and (b) with feedback.
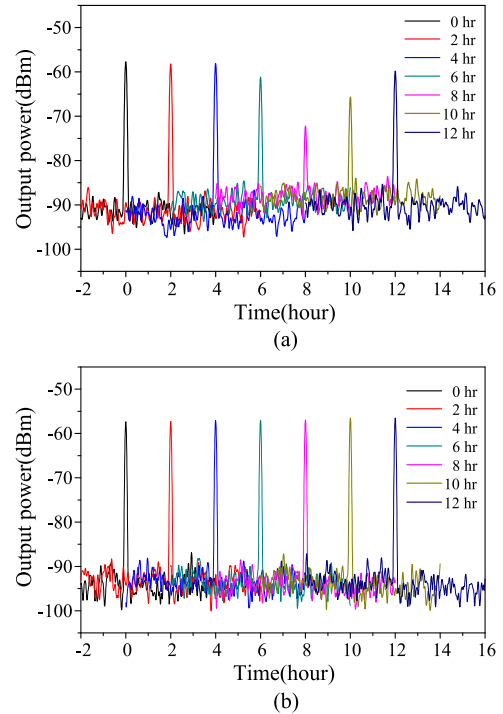

Fig. 10. Power spectrum of the AC component for an applied acoustic pressure of 10 mPa at 10 kHz. (a) without feedback and (b) with feedback.
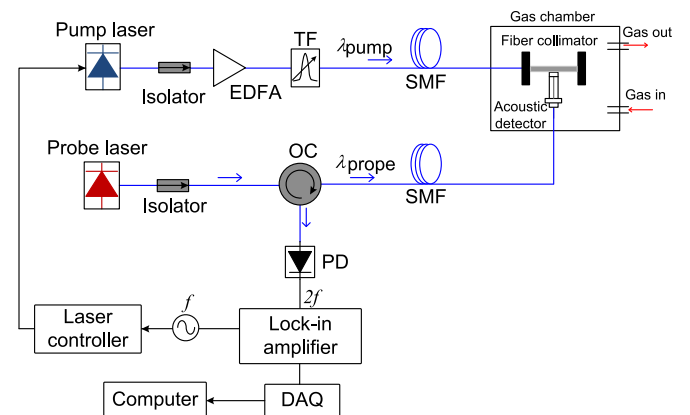

Fig. 11. Setup of the PAS system for acetylene detection. Blue line, optical fiber; black line, electrical cable; TF, tunable filter; OC, optical circulator; PD, photo-detector; DAQ, data acquisition; DFB, distributed feedback laser (the pump); ECDL, external-cavity diode laser (the probe); EDFA, erbium-doped fibre amplifier; Filter (TF) is used to minimize the effect of EDFA's ASE noise.

and an optical tunable filter with tunable range from 1530 to 1565 nm and a bandwidth of 0.3 nm. The output electrical signal from the PD contains both AC and DC components, which are separated by use of an electrical filter (Model SR650, Stanford research systems, Inc.). The high-pass AC signal is transferred to ESA for acoustic detection while the low-pass DC signal is delivered to the data acquisition card (DAQ) and recorded in real-time by a computer. The DC component depends on the operation point and can be used to form a feedback loop for Q-point stabilization through tuning the wavelength of the tunable optical filter by a Labview program.

We firstly measured the DC and AC components without using feedback control. The applied acoustic pressure level is 10 mPa and the frequency is 10 kHz. Figs. 9(a) and 10(a) show respectively the recorded DC and AC output voltage. The DC output varies between 0.5 V and 1.2 V over 12 hours, indicating the operating point has changed. For constant applied acoustic pressure, the AC output changed by over 10 dB from above -60 dBm to below -70 dBm, showing the demodulation is instable.

We then measured the output signals over a similar period by using feedback to stabilize the operating point. To set the operating point, the optical tunable filter firstly scans several free spectrum range (FSR) of the interference fringe to obtain the maximum and minimum DC values of the reflected spectrum, from which we can determine the output DC voltage corresponding to the Q point. The wavelength of the filter is then tuned to work around that point. When the operating point is drifted, the DC output voltage will vary accordingly, then the Labview program will tune wavelength of the filter so that the operating point is maintained.

Figs. 9(b) and 10(b) show the DC and AC output voltages over a 12-hour period with feedback loop on. The use of active feedback significantly improves the long term stability of the demodulation system and for a constant acoustic pressure of 10 mPa, the AC output remained in a stable level of -58 dBm.

The stable operation of the acoustic detector would enable PAS gas sensors with better stability since the PA signal itself would not affect the operating point of the Fabry-Perot.

V. GAS DETECTION EXPERIMENTS

A. Resonant and Non-Resonant Detection

PAS gas (acetylene) detection experiments with the fiber acoustic detectors operating at resonant and non-resonant mode were conducted using the setup shown in Fig. 11. A distributed

feedback (DFB) semiconductor laser is used as the pump source (λ_{pump}) and its wavelength is tuned across the P (13) absorption line of acetylene (C_2H_2) at 1532.830 nm. The pump laser was collimated to a beam diameter of –300 μm and its wavelength is modulated sinusoidally at a frequency of 22.8 kHz, corresponding to one of the resonances of the acoustic detector. The amplitude of wavelength modulation was set to –2.2 times of the absorption linewidth in order to maximize the second-harmonic signal [57]. The modulated pump light was absorbed by gas sample and the generated PA signal is detected by use of the same acoustic detector with diameter of –2.5 mm as described in Section IV, Part A. The acoustic wave induced periodic diaphragm deflection, which was probed by an external cavity diode laser (ECDL) with output power of –1 mW. The wavelength of the probe laser (λ_{prope}) is tuned to 1551.9 nm, corresponding to steepest slope of the interference, which produces the largest change in output power for a given acoustically induced vibration. The reflected probe light from the detector travels back along the same fiber and was detected by a photo-detector (PD). The output from the PD is demodulated by a lock-in amplifier (Stanford research systems, SR830) at its second harmonic frequency (i.e., 45.6 kHz). The time constant of the lock-in amplifier is set to 10 s with a filter slope of 18 dB Oct^{-1}. All the experiments were carried out at atmospheric pressure and room temperature.

Fig. 12(a) shows the second harmonic lock-in outputs for different pump power levels delivered to the fiber collimator when the pump wavelength was tuned across the P(13) line of acetylene. The space within the collimator was filled with 100 p.p.m. acetylene balanced by nitrogen (N_2). For the pump power of 45.1 mW, the peak-to-peak amplitude of the second harmonic signal is –38.2 μV. The second harmonic lock-in output when the pump is tuned away from the absorption peak to 1,532.93 nm is shown in Fig. 12(b). The standard deviation (s.d.) of the noise over 8-min duration is 0.16 μV, not much larger than the noise level (0.11 μV) when the pump is off, giving a signal to noise ratio (SNR) of 238. So the lower detection limit for a signal to noise ratio of unity is estimated to be 418 ppb in NEC for a detection bandwidth of 0.0094 Hz. The second harmonic signal and the standard deviation (s.d.) of the noise as functions of pump power level are shown in Fig. 12(c). The second harmonic output signals for different pump power levels are shown in black squares. Curve fitting shows that it has a linear relationship ($r^2 = 0.9960$) with the pump power in the range of 17 to 45 mW. The s.d. of the noise as functions of pump power levels are shown min blue squares, showing that the noise level remained in a relatively plane level.

We also carried out investigation on the effect of varying modulation frequency on the amplitude of the second harmonic output signal. The modulation frequency of DFB pump laser was varied from 21 kHz to 25 kHz and the second harmonic lock-in signal is shown in Fig. 13. The power of the pump laser is fixed to 45 mW. The output signal is maximized at –22.8 kHz, corresponding to the resonant frequency of the graphene nano-mechanical resonator [53]. The Q-factor of the resonance is defined as $Q = f_0/\Delta f$, where the values of f_0 and Δf are obtained by fitting the measured resonant peak using
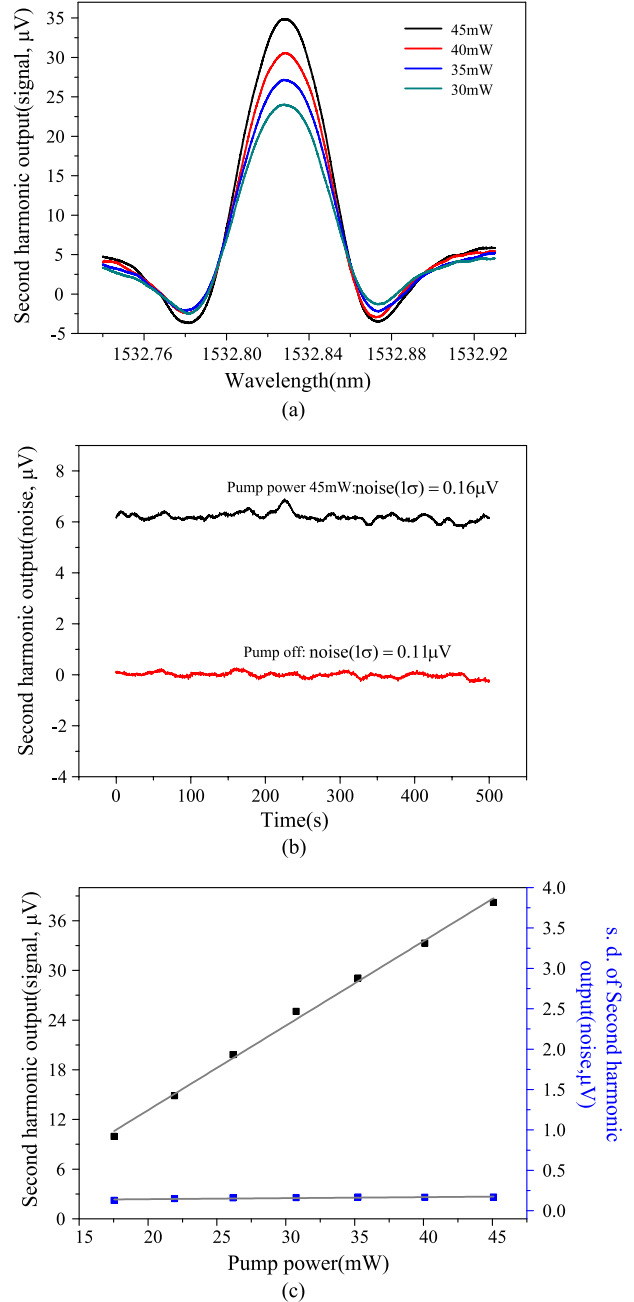

(a)

(b)

(c)

Fig. 12. Experimental results for the acetylene detection. (a) Second harmonic lock-in output (signal) when pump laser is tuned across the P(13) line of acetylene at 1,532.83 nm under different pump power levels. (b) Second harmonic lock-in output when the pump wavelength is tuned away from absorption and to 1,532.93nm. Black line: pump power is –45.1 mW. Red line: pump power is zero (off). (c) Second harmonic signal and the s.d. of the noise as functions of pump power level. The time constant of the lock-in amplifier is 10 s with a filter slope of 18 dB Oct^{-1}. The gas concentration used is 100 ppm acetylene, and the experiments were conducted at room temperature.

the Lorentz function. The Q value of this graphene resonator is calculated to be 13. To compare the performance of the PAS gas sensor operating at the resonant and non-resonant frequencies, we evaluated signals and the noises at 22.84 kHz (at resonance) and 21.05 kHz (off resonance), and they are shown in Table III. The SNR of the PA gas sensor at resonance is –10 times
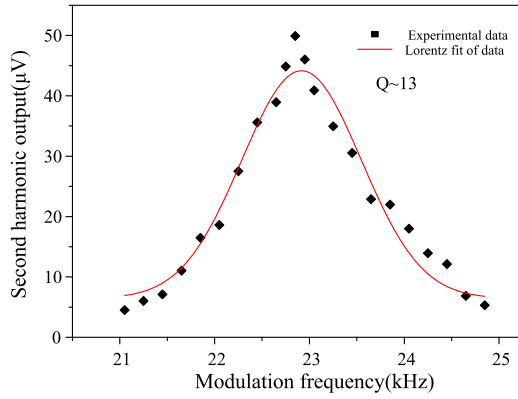
Fig. 13. Second harmonic lock-in output under different modulation frequencies when the pump laser is tuned to the P(13) absorption line and fixed to 1532.83 nm. Black squares: Experimental data. Red line: Lorentz fitting of the Data. The gas (acetylene) concentration is 100 ppm.
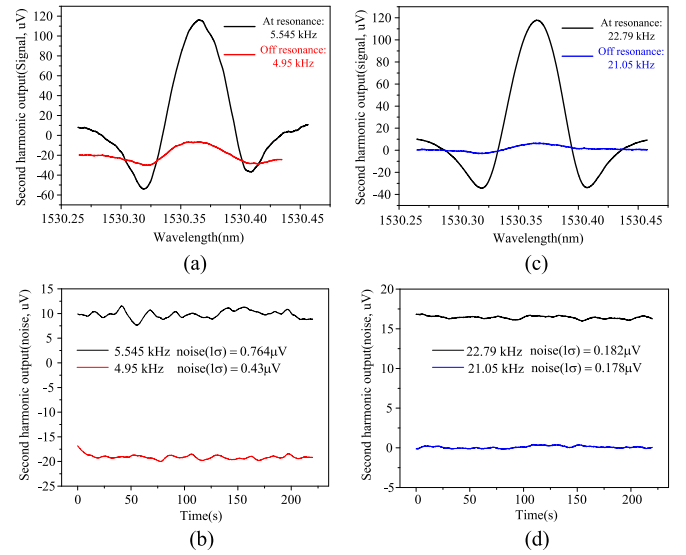

Fig. 14. Experimental results for the acetylene detection at two specific resonances around (a, b) 5 kHz and (c, d) 22 kHz. (a) Second harmonic lock-in output (signal) at resonance of 5.545 kHz (black curve) and off resonance of 4.95 kHz (red curve).(b) Second harmonic lock-in output (noise) when the pump wavelength is tuned away from the absorption peak to 1,530.26 nm at acoustic resonance of 5.545 kHz (black curve) and off acoustic resonance of 4.95 kHz (red curve). (c) Second harmonic lock-in output (signal) at resonance of 22.79 kHz (black curve) and off resonance of 21.05 kHz (blue curve). (d) Second harmonic lock-in output (noise) when the pump wavelength is tuned away from the absorption peak to 1,530.26 nm at resonance of 22.79 kHz (black curve) and off resonance of 21.05 kHz (blue curve).

TABLE III
PERFORMANCE OF GAS SENSOR FOR TWO DIFFERENT
MODULATION FREQUENCIES

Modulation frequency	22.84 kHz (at resonance)	21.05 kHz (off resonance)
2nd harmonic output at absorption peak (1532.83 nm)	49.92 μV	4.49 μV
2nd harmonic output away from absorption peak (1532.93 nm)	5.62 μV	1.17 μV
s.d. of noise over 500 s	0.169 μV	0.128 μV
SNR	262	25
NEC	0.381ppm	4 ppm

better than that off resonance, showing the system performance can be significantly improved by operating the graphene diaphragm at resonance. The lower detection limit at the resonance (22.84 kHz) for SNR = 1 is estimated to be 381 ppb, which is –10 times better than that off resonance and in accordance with the calculated Q factor of 13.

B. Operating at Different Acoustic Resonances

The performances of the PAS gas sensor operating at two acoustic resonances around 5 and 22 kHz were also investigated. The experimental setup is similar to that shown in Fig. 11, but a different DFB laser with its wavelength tuned to the P(9) absorption line acetylene centered at 1530.371 nm. The pump power used is 123.9 mW and acetylene concentration of 100 ppm. The time constant of the lock-in amplifier is set to 3 s with a filter slope of 18 dB/Oct. Fig. 14 shows the second harmonic lock-in output when the pump wavelength is scanned across the P(9) line and when the pump laser is modulated around 5 and 22 kHz. The peak to peak value of the second harmonic outputs are similar at 5 and 22 kHz which are around 160 μV. However, the noise level at 5 kHz is –4 times larger than that at 22 kHz. The NEC and NNEA values at 22 kHz are calculated to be 119.8 ppb and 9.782×10^{-8} cm^{-1}WHz$^{-1/2}$. Table IV shows the

signals and the noises at different modulation frequencies and at different pump wavelength. The detection sensitivity can be improved by operating the graphene diaphragm at a resonance with a higher resonance frequency since the SNR is better at higher frequencies due to probably smaller environmental noise.

C. Improvement of Detection Sensitivity

The performance of the optical fiber PAS gas sensor may be further improved by using a nano-mechanical resonator with a higher Q-factor. The graphene diaphragm can be regarded as a thin circular plate with radius r and thickness t which is clamped around its edges and vibrates. Considering that the graphene diaphragm is in contact with a Newtonian fluid (air), the Q-factor (Q_{tot}) contains two terms concerning about the effect of acoustic radiation and viscous damping, so Q_{tot} of the resonator may be expressed as [49], [58], [59]

$$Q_{tot} = \frac{1}{1/Q_{ar} + 1/Q_{vis}} \tag{3}$$

where Q_{ar} and Q_{vis} are the Q-factor of acoustic radiation and viscosity term, respectively,with

$$Q_{ar} = 1.20 \frac{\rho_p c_f}{\rho_f c_p}(1+\beta)^{3/2} Q_{vis} = \frac{0.95}{\xi}\left(\frac{1}{\beta}+1\right) \tag{4}$$

where $\xi = \sqrt{\frac{v}{\omega_1 r^2}}$ is a non-dimensional parameter, and v is the kinetic viscosity of the fluid. Taking the fundamental mode of

Modulation frequency	2nd harmonic output at absorption peak(1530.371 nm)	2nd harmonic output away from absorption peak(1530.26 nm)	2nd harmonic output signal	s.d. of noise over 200 s	SNR	NEC (ppm)	NNEA (cm^{-1}WHz$^{-1/2}$)
5.545 kHz (at resonance)	115.66 μV	−52.57 μV	168.2 μV	0.764 μV	220	0.45	3.707 × 10^{-7}
4.95 kHz (off resonance) (off resonance)	−6.50 μV	−30.04 μV	23.54 μV	0.430 μV	55	1.83	1.492 × 10^{-6}
22.79 kHz (at resonance)	117.70 μV	−34.21 μV	151.9 μV	0.182 μV	835	0.1198	9.782 × 10^{-8}
21.05 kHz (off resonance)	6.27 μV	−2.88 μV	9.15 μV	0.178 μV	51	1.944	1.587 × 10^{-6}

NNEA, Normalized noise equivalent absorption coefficient; NEC, noise equivalent concentration

TABLE V
PHYSICAL PARAMETERS OF GRAPHENE DIAPHRAGM AND AIR

Graphene diaphragm	*Diameter 2r (mm)*: 2.5	*Density ρ_p (kg/m^3)*: 2200
	Thickness t (nm): 100	*Poisson ratio ν*: 0.17
	Young's modulus E:	~1 TPa
Air (at 1atm,	*Dynamic viscosity μ (Pa·s)*: 1.8 × 10^{-5}	*Density ρ_f (kg/m^3)*: 1.18
(room temperature)	*Kinetic viscosity υ (m^2/s)*: 1.53 × 10^{-5}	*Speed of sound c_f (m/s)*: 343

vibration as an example, ω_1 can be expressed as

$$\omega_1 = \frac{10.21}{\sqrt{12(1+\beta)}} \frac{t c_p}{r^2} \quad (5)$$

where c_p is the velocity of propagation of waves in the plate, and β is the added virtual mass factor, with

$$c_p = \sqrt{\frac{E}{(1-\nu^2)\rho_p}}; \beta = 0.6689 \frac{\rho_f r}{\rho_p t} \quad (6)$$

where E, ν, and ρ_p are the Young's modulus, Poisson's ratio and mass density of graphene diaphragm, ρ_f is the density of the surrounding fluid.

We employed Eq. (3) to theoretically calculate the Q-factor of the graphene in air at atmospheric pressure and room temperature. In the calculations, we used the physical parameters of the graphene diaphragm and air listed in Table V [49], [58]. For a graphene diaphragm with radius of 1.25 mm and thickness of 100 nm, Q_{ar} and Q_{vis} are calculated to be 455 and 15, respectively, so the Q_{tot} value is 14 of the diaphragm. This result clarifies that the viscous damping term does play an important role in the Q_{tot} value of the diaphragm that vibrates at atmospheric pressure. When the pressure decreases below 1 Pa, the air damping term can be negligible compared to the intrinsic damping of the vibrating diaphragm and the Q-factor may increase significantly [60]. We can infer that the Q-factor in vacuum would become 455 or larger, then the lower detection limit for gas detection would below − 4.2 ppb. Therefore the performances of the PA gas sensor may be improved by increasing the Q-factor value at lower pressures to achieve ppb level detection sensitivity.

VI. CONCLUSION

In summary, we demonstrated an all-optical fiber PA spectrometric gas sensor with a 100-nm-thick, 2.5-mm-diameter multilayer graphene nano-mechanical resonator as the acoustic detector. By operating at the resonance of the nano-mechanical resonator, the SNR is enhanced, and a lower detection limit for acetylene with the NEC of 119.8 ppb and NNEA of 9.782 × 10^{-8} cm^{-1}WHz$^{-1/2}$ are achieved. Theoretical calculation demonstrates that the performances of the PA gas sensor can be further enhanced by increasing the Q-factor value at lower pressures to achieve ppb level detection sensitivity. Compared with previously reported PAS systems, a nano-mechanical resonator is used as acoustic detector in our system, which improves the SNR by 13 times, indicating higher gas detection sensitivity can be achieved by using lower pump power. Moreover, the resonator is built at the end of an optical fiber, which allows the use of optical fiber interferometer to interrogate it and enables all-fiber PAS gas detection systems. The all-fiber photoacoustic gas sensor is immune to electromagnetic interference and would be ideally suited for remote, and multipoint detection in a multiplexed fiber optic sensor network.

The performance of optical fiber PAS system for gas detection can be further improved by increasing the power of the pump beam since the PA signal is proportional to the pump power level, and by using a larger-diameter graphene nano-mechanical resonator to increase the acoustic detection sensitivity. A resonant PA cell with its acoustic resonant frequency matched to that of the nano-mechanical resonator could also be used to further enhance the gas detection sensitivity.

The realization of this simple, compact, and sensitive all-optical gas sensor has a great potential in a range of important applications such as breath analysis for medical diagnosis and condition monitoring of oil-filled electrical power transformers.

REFERENCES

[1] A. Miklós, P. Hess, and Z. Bozóki, "Application of acoustic resonators in photoacoustic trace gas analysis and metrology," *Rev. Sci. Instrum.*, vol. 72, no. 4, pp. 1937–1955, Apr. 2001.

[2] T. Schmid, "Photoacoustic spectroscopy for process analysis," *Anal. Bioanal. Chem.*, vol. 384, no. 5, pp. 1071–1086, 2006.

[3] A. Elia, P. M. Lugarà, C. Di Franco, and V. Spagnolo, "Photoacoustic techniques for trace gas sensing based on semiconductor laser sources," *Sensors*, vol. 9, no. 12, pp. 9616–9628, Dec. 2009.

[4] M. Viegerov, "Eine Methode der gasanalyse, beruhend auf der optisch-akustischen tyndall-röntgenerscheinung," *Dokl. Akad. Nauk SSSR*, vol. 19, pp. 687–688, 1938.

[5] E. L. Kerr and J. G. Atwood, "The laser illuminated absorptivity spectrophone: A method for measurement of weak absorptivity in gases at laser wavelengths," *Appl. Opt.*, vol. 7, no. 5, pp. 915–921, May 1968.

[6] L. Kreuzer, "Ultralow gas concentration infrared absorption spectroscopy," *J. Appl. Phys.*, vol. 42, no. 7, pp. 2934–2943, Jun. 1971.

[7] L. Kreuzer, N. Kenyon, and C. Patel, "Air pollution: Sensitive detection of ten pollutant gases by carbon monoxide and carbon dioxide lasers," *Science*, vol. 177, no. 4046, pp. 347–349, Jul. 1972.

[8] M. B. Pushkarsky *et al.*, "High-sensitivity detection of TNT," *Proc. Nat. Acad. Sci.*, vol. 103, no. 52, pp. 19630–19634, Dec. 2006.

[9] P. A. Martin, "Near-infrared diode laser spectroscopy in chemical process and environmental air monitoring," *Chem. Soc. Rev.*, vol. 31, no. 4, pp. 201–210, Jun. 2002.

[10] C. Dewey, Jr., R. Kamm, and C. Hackett, "Acoustic amplifier for detection of atmospheric pollutants," *Appl. Phys. Lett.*, vol. 23, no. 11, pp. 633–635, Dec.1973.

[11] R. D. Kamm, "Detection of weakly absorbing gases using a resonant optoacoustic method," *J. Appl. Phys.*, vol. 47, no. 8, pp. 3550–3558, Aug. 1976.

[12] L.-G. Rosengren, "Optimal optoacoustic detector design," *Appl. Opt.*, vol. 14, no. 8, pp. 1960–1976, Aug.1975.

[13] C. Patel and R. Kerl, "A new optoacoustic cell with improved performance," *Appl. Phys. Lett.*, vol. 30, no. 11, pp. 578–579, Jun. 1977.

[14] R. Gerlach and N. Amer, "Brewster window and windowless resonant spectrophones for intracavity operation," *Appl. Phys.*, vol. 23, no. 3, pp. 319–326, Jul. 1980.

[15] S. Bernegger and M. Sigrist, "Longitudinal resonant spectrophone for CO-laser photoacoustic spectroscopy," *Appl. Phys. B*, vol. 44, no. 2, pp. 125–132, Apr. 1987.

[16] F. Harren, J. Reuss, E. Woltering, and D. Bicanic, "Photoacoustic measurements of agriculturally interesting gases and detection of C_2H_4 below the ppb level," *Appl. Spectrosc.*, vol. 44, no. 8, pp. 1360–1368, Mar. 1990.

[17] F. Harren, F. Bijnen, J. Reuss, L. Voesenek, and C. Blom, "Sensitive intracavity photoacoustic measurements with a CO_2 waveguide laser," *Appl. Phys. B*, vol. 50, no. 2, pp. 137–144, Jun. 1990.

[18] P. Meyer and M. Sigrist, "Atmospheric pollution monitoring using CO_2-laser photoacoustic spectroscopy and other techniques," *Rev. Sci. Instrum.*, vol. 61, no. 7, pp. 1779–1807, Jul. 1990.

[19] Z. Bozóki *et al.*, "Intracavity photoacoustic gas detection with an external cavity diode laser," *Appl. Phys. B*, vol. 63, no. 4, pp. 399–401, Apr. 1996.

[20] A. Boschetti *et al.*, "Resonant photoacoustic simultaneous detection of methane and ethylene by means of a 1.63-μm diode laser," *Appl. Phys. B*, vol. 74, no. 3, pp. 273–278, Feb. 2002.

[21] M. E. Webber, M. Pushkarsky, and C. K. N. Patel, "Fiber-amplifier-enhanced photoacoustic spectroscopy with near-infrared tunable diode lasers," *Appl. Opt.*, vol. 42, no. 12, pp. 2119–2126, Apr. 2003.

[22] J. Li, X. Gao, L. Fang, W. Zhang, and H. Cha, "Resonant photoacoustic detection of trace gas with DFB diode laser," *Opt. Laser Technol.*, vol. 39, no. 6, pp. 1144–1149, 2007.

[23] Y. Peng, W. Zhang, L. Li, and Q. Yu, "Tunable fiber laser and fiber amplifier based photoacoustic spectrometer for trace gas detection," *Spectrochim. Acta A*, vol. 74, no. 4, pp. 924–927, Aug. 2009.

[24] L.-Y. Hao *et al.*, "Cylindrical mirror multipass Lissajous system for laser photoacoustic spectroscopy," *Rev. Sci. Instrum.*, vol. 73, no. 5, pp. 2079–2085, May 2002.

[25] J. Rey, D. Marinov, D. Vogler, and M. Sigrist, "Investigation and optimisation of a multipass resonant photoacoustic cell at high absorption levels," *Appl. Phys. B*, vol. 80, no. 2, pp. 261–266, 2005.

[26] J. Saarela, J. Sand, T. Sorvajärvi, A. Manninen, and J. Toivonen, "Transversely excited multipass photoacoustic cell using electromechanical film as microphone," *Sensors*, vol. 10, no. 6, pp. 5294–5307, May 2010.

[27] Y. Cao *et al.*, "Multi-pass absorption spectroscopy for H_2O_2 detection using a CW DFB-QCL," *Adv. Opt. Technol.*, vol. 3, no. 5–6, pp. 549–558, Dec. 2014.

[28] A. Rossi *et al.*, "Optical enhancement of diode laser-photoacoustic trace gas detection by means of external Fabry-Perot cavity," *Appl. Phys. Lett.*, vol. 87, no. 4, Jul. 2005, Art. no. 041110.

[29] M. Hippler, C. Mohr, K. A. Keen, and E. D. McNaghten, "Cavity-enhanced resonant photoacoustic spectroscopy with optical feedback cw diode lasers: A novel technique for ultratrace gas analysis and high-resolution spectroscopy," *J. Chem. Phys.*, vol. 133, no. 4, Jul. 2010, Art. no. 044308.

[30] A. A. Kosterev, Y. A. Bakhirkin, R. F. Curl, and F. K. Tittel, "Quartz-enhanced photoacoustic spectroscopy," *Opt. Lett.*, vol. 27, no. 21, pp. 1902–1904, Nov. 2002.

[31] A. A. Kosterev and F. K. Tittel, "Ammonia detection by use of quartz-enhanced photoacoustic spectroscopy with a near-IR telecommunication diode laser," *Appl. Opt.*, vol. 43, no. 33, pp. 6213–6217, Nov. 2004.

[32] A. A. Kosterev, F. K. Tittel, D. V. Serebryakov, A. L. Malinovsky, and I. V. Morozov, "Applications of quartz tuning forks in spectroscopic gas sensing," *Rev. Sci. Instrum.*, vol. 76, no. 4, Apr. 2005, Art. no. 043105.

[33] K. Liu *et al.*, "Off-beam quartz-enhanced photoacoustic spectroscopy," *Opt. Lett.*, vol. 34, no. 10, pp. 1594–1596, May 2009.

[34] K. Liu *et al.*, "Trace gas detection based on off-beam quartz enhanced photoacoustic spectroscopy: Optimization and performance evaluation," *Rev. Sci. Instrum.*, vol. 81, no. 10, Oct. 2010, Art. no. 103103.

[35] L. Dong, A. A. Kosterev, D. Thomazy, and F. K. Tittel, "QEPAS spectrophones: Design, optimization, and performance," *Appl. Phys. B*, vol. 100, no. 3, pp. 627–635, May 2010.

[36] J. Kauppinen, K. Wilcken, I. Kauppinen, and V. Koskinen, "High sensitivity in gas analysis with photoacoustic detection," *Microchem. J.*, vol. 76, no. 1, pp. 151–159, 2004.

[37] T. Laurila, H. Cattaneo, V. Koskinen, J. Kauppinen, and R. Hernberg, "Diode laser-based photoacoustic spectroscopy with interferometrically-enhanced cantilever detection," *Opt. Express*, vol. 13, no. 7, pp. 2453–2458, Apr. 2005.

[38] T. Laurila, H. Cattaneo, V. Koskinen, J. Kauppinen, and R. Hernberg, "Diode laser-based photoacoustic spectroscopy with interferometrically-enhanced cantilever detection: Erratum," *Opt. Express*, vol. 14, no. 9, p. 4195, May 2006.

[39] V. Koskinen, J. Fonsen, K. Roth, and J. Kauppinen, "Cantilever enhanced photoacoustic detection of carbon dioxide using a tunable diode laser source," *Appl. Phys. B*, vol. 86, no. 3, pp. 451–454, Jan. 2007.

[40] V. Koskinen, J. Fonsen, K. Roth, and J. Kauppinen, "Progress in cantilever enhanced photoacoustic spectroscopy," *Vibrational Spectrosc.*, vol. 48, no. 1, pp. 16–21, Feb. 2008.

[41] D. Leslie, G. Trusty, A. Dandridge, and T. Giallorenzi, "Fibre-optic spectrophone," *Electron. Lett.*, vol. 17, no. 17, pp. 581–582, Aug. 1981.

[42] J. Breguet, J.-P. Pellaux, and N. Gisin, "Photoacoustical detection of trace gases with an optical microphone," in *Proc. Int. Conf. Optical Fiber Sensors Conf.*, 1994, pp. 457–460.

[43] Q. Wang, J. Wang, L. Li, and Q. Yu, "An all-optical photoacoustic spectrometer for trace gas detection," *Sens. Actuators B: Chem.*, vol. 153, no. 1, pp. 214–218, Oct. 2011.

[44] Y. Cao, W. Jin, H. L. Ho, and J. Ma, "Miniature fiber-tip photoacoustic spectrometer for trace gas detection," *Opt. Lett.*, vol. 38, no. 4, pp. 434–436, Feb. 2013.

[45] P. Beard, F. Perennes, E. Draguioti, and T. Mills, "Optical fiber photoacoustic–photothermal probe," *Opt. Lett.*, vol. 23, no. 15, pp. 1235–1237, Sep. 1998.

[46] O. C. Akkaya, O. Kilic, M. J. Digonnet, G. S. Kino, and O. Solgaard, "High-sensitivity thermally stable acoustic fiber sensor," in *Proc. IEEE Sensors*, 2010, pp. 1148–1151.

[47] F. Xu *et al.*, "High-sensitivity Fabry-Perot interferometric pressure sensor based on a nanothick silver diaphragm," *Opt. Lett.*, vol. 37, no. 2, pp. 133–135, Jan. 2012.

[48] F. Guo *et al.*, "High-sensitivity, high-frequency extrinsic Fabry-Perot interferometric fiber-tip sensor based on a thin silver diaphragm," *Opt. Lett.*, vol. 37, no. 9, pp. 1505–1507, May 2012.

[49] J. Ma *et al.*, "Fiber-optic Fabry-Perot acoustic sensor with multilayer graphene diaphragm," *IEEE Photon. Technol. Lett.*, vol. 25, no. 10, pp. 932–935, May 2013.

[50] P. Patimisco, G. Scamarcio, F. K. Tittel, and V. Spagnolo, "Quartz-enhanced photoacoustic spectroscopy: A review," *Sensors*, vol. 14, no. 4, pp. 6165–6206, Mar. 2014.

[51] C. Lee, X. Wei, J. W. Kysar, and J. Hone, "Measurement of the elastic properties and intrinsic strength of monolayer graphene," *Science*, vol. 321, no. 5887, pp. 385–388, Jun. 2008.

[52] J. Ma, W. Jin, H. L. Ho, and J. Y. Dai, "High-sensitivity fiber-tip pressure sensor with graphene diaphragm," *Opt. Lett.*, vol. 37, no. 13, pp. 2493–2495, Jul. 2012.

[53] J. Ma, W. Jin, H. Xuan, C. Wang, and H. L. Ho, "Fiber-optic ferrule-top nanomechanical resonator with multilayer graphene film," *Opt. Lett.*, vol. 39, no. 16, pp. 4769–4772, Aug. 2014.

[54] J. Ma, Y. Yu, and W. Jin, "Demodulation of diaphragm based acoustic sensor using Sagnac interferometer with stable phase bias," *Opt. Express*, vol. 23, no. 22, pp. 29268–29278, Nov. 2015.

[55] J. Ma, J. Ju, L. Jin, and W. Jin, "A compact fiber-tip micro-cavity sensor for high-pressure measurement," *IEEE Photon. Technol. Lett.*, vol. 23, no. 21, pp. 1561–1563, Nov. 2011.

[56] B. Yu, D. W. Kim, J. Deng, H. Xiao, and A. Wang, "Fiber Fabry-Perot sensors for detection of partial discharges in power transformers," *Appl. Opt.*, vol. 42, no. 16, pp. 3241–3250, Jun. 2003.

[57] S. Schilt, L. Thevenaz, and P. Robert, "Wavelength modulation spectroscopy: Combined frequency and intensity laser modulation," *Appl. Opt.*, vol. 42, no. 33, pp. 6728–6738, Nov. 2003.

[58] M. Olfatnia *et al.*, "Medium damping influences on the resonant frequency and quality factor of piezoelectric circular microdiaphragm sensors," *J. Micromech. Microeng.*, vol. 21, no. 4, Feb. 2011, Art. no. 045002.

[59] H. Lamb and R. Southwell, "The vibrations of a spinning disk," *Proc. R. Soc. London.* vol. 99, no. 699, pp. 272–280, Apr. 1921.

[60] F. Blom, S. Bouwstra, M. Elwenspoek, and J. Fluitman, "Dependence of the quality factor of micromachined silicon beam resonators on pressure and geometry," *J. Vacuum Sci. Technol. B*, vol. 10, no. 1, pp. 19–26, Jan. 1992.

Yanzhen Tan received the B.Sc. degree from the China University of Mining and Technology, Beijing, China, in 2011, and the M.Eng. degree from Jinan University, Guangdong, China, in 2014. She is currently working toward the Ph.D. degree in Prof. Wei Jin's Group in the Department of Electrical Engineering, The Hong Kong Polytechnic University, Kowloon, Hong Kong. Her research interests include gas sensing with optical fibers, photonic crystal fibers, fiber optic sensors, and devices.

Congzhe Zhang received the B.Sc. and M.Eng. degrees from Hebei University, Hebei, China, in 2009 and 2013, respectively. He is currently working toward the Ph.D. degree at Beihang University, Beijing, China. He is also a Research Assistant in Prof. Wei Jin's Group in the Department of Electrical Engineering, The Hong Kong Polytechnic University, Kowloon, Hong Kong. His research interests include gas sensing with optical fibers, fiber optic sensors, and devices.

Wei Jin received the B.Eng. and M.Sc. degrees from the Beijing University of Aeronautics and Astronautics, Beijing, China, in 1984 and 1987, respectively, and the Ph.D. degree in fiber optics from the University of Strathclyde, Glasgow, U.K., in 1991, where he was employed as a Postdoctoral Research Fellow till the end of 1995. He joined the Department of Electrical Engineering, The Hong Kong Polytechnic University, Kowloon, Hong Kong, as an Assistant Professor in 1996 and was promoted to an Associate Professor in 1998 and a Professor in 2003. He is currently a Chair Professor of photonic instrumentation at The Hong Kong Polytechnic University. His research interests include photonic crystal fibers and devices, optical fiber sensors, fiber lasers and amplifiers, optical gas detectors, condition monitoring of electrical power transformers, and civil and mechanical structures.

Fan Yang received the B.Eng. and M.Eng. degrees from the Huazhong University of Science and Technology, Hubei, China, in 2008 and 2011, respectively, and the Ph.D. degree from The Hong Kong Polytechnic University, Kowloon, Hong Kong, in 2015, where he is currently a Postdoctoral Research Fellow. His research interests include gas sensing with optical fibers, photonic crystal fibers, and fiber optic sensors and devices.

Hoi Lut Ho received the B.Eng. and Ph.D. degrees from The Hong Kong Polytechnic University, Kowloon, Hong Kong, in 1997 and 2002, respectively. He is currently working as a Scientific Officer in The Hong Kong Polytechnic University. He has published more than 30 technical papers in international refereed journals as well as international conferences. His research interests include fiber optic sensors, multiplexing techniques in optical sensing system, fiber Bragg grating sensors, and photonic crystal fiber sensors and devices.

Jun Ma received the B.Eng. degree from Huazhong University of Science and Technology, Hubei, China, in 2010, and the Ph.D. degree from The Hong Kong Polytechnic University, Kowloon, Hong Kong, in 2014. He is currently a Postdoctoral Research Fellow at Washington University at St. Louis, St. Louis, MO, USA.